INFLUENCE OF ABDOMINAL AORTIC ANEURYSM SHAPE ON HEMODYNAMICS

R.J. Lozowy[1], D.C.S. Kuhn[1] and A.J. Boyd[2]

[1] *Department of Mechanical Engineering, University of Manitoba, MB, Canada*
[2] *Department of Vascular Surgery, University of Manitoba, MB, Canada*
umlozowy@cc.umanitoba.ca

Abstract

Direct numerical simulation was performed on two patient-specific abdominal aortic aneurysms (AAA) using physiologically realistic flow conditions. The patients have AAA with diameters of approximately 5 and 7 cm, respectively. The blood flow hemodynamics are shown to consist of large-scale periodic structures and the flow transitions from laminar-to-turbulent and back to laminar during a pulse. Transition does not occur until after the maximum flow rate has been reached and turbulence persists in the AAA after the bulk flow decelerates to a laminar condition. For both cases, a jet of blood forms at the AAA throat and impinges against the arterial wall at the site of maximal aortic diameter. During the pulse structures shear across the AAA causing locally high wall shear stress (WSS). It is shown that the cases have significantly different hemodynamics. The smaller sized AAA has faster moving flow structures, higher WSS, higher turbulent kinetic energy, and the blood spirals down the AAA toward the iliac arteries. In the larger sized AAA, the blood flow channels down on the anterior side and a large recirculation zone forms on the posterior side. A large recirculation zone causes low WSS which is know to promote atherosclerosis.

1 Introduction

The vascular condition known as abdominal aortic aneurysm (AAA) is a dilatation of at least 1.5 times the diameter of the aortic segment between the renal arteries and the iliac bifurcation. The aorta is the longest artery in the human body and is approximately $2 - 2.4$ cm in diameter. The AAA dilatation weakens the arterial wall making it susceptible to rupture. Most AAA continue to enlarge progressively and the risk of rupture is related to size. To prevent rupture, AAA are repaired when they meet a size criteria of 5.5 cm in men and 5 cm in women and since the mortality-associated risk of rupture is less than the risks posed by surgical repair for patients below the diameter criteria, most patients with small aneurysms post-pone surgery; however, as many as 33% of ruptured AAA have diameters smaller than 5 cm. Currently, there is no truly reliable way to evaluate susceptibility of particular AAA to rupture and diameter is one of many
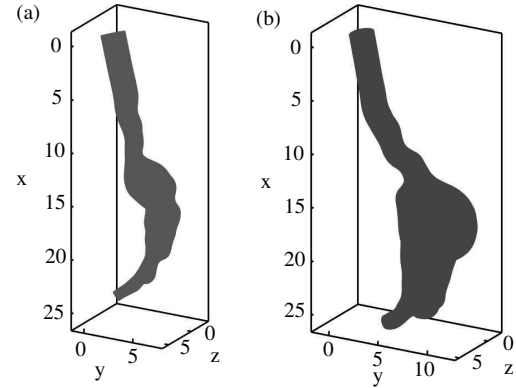

Figure 1: Geometry for (a) case 1 and (b) case 2. Units are in cm.

criteria that could be used to determine when to operate on an AAA. Discovery of these evaluation criteria would vastly improve AAA management and decrease mortality.

AAA formation and growth occurs due to a combination of biological and hemodynamic factors (Lasheras 2010). A known hemodynamic factor is the frictional drag exerted by blood flow on the arterial wall, referred to as wall shear stresses (WSS). Stable unidirectional WSS is associated with healthy, intact vascular endothelium, whereas low flow with oscillating WSS is associated with atherosclerosis (Tarbell et al. 2014). Evidence also suggests that high WSS with sharp spacial gradients (Dolan et al. 2012) can damage the arterial wall. Low oscillating WSS is primarily caused by zones of recirculating blood and high WSS by blood flow impingement. Since the abdominal aorta is generally a uniform cylindrical is shape in most cases the flow would remain laminar. However the shape of an AAA could cause the blood flow to transition-to-turbulence increasing the oscillation in the flow direction and causing higher WSS. The influence of vascular shape on turbulence is not well understood and the goal of this study is to numerically calculate physiological blood flow in two patient-specific AAA to determine if there is a notable different in the flow structures and turbulence intensity between the cases. Previous work on physiological blood flow in patient-specific arteries includes the experimental

study by Stamatopoulos et al. (2011) and the numerical study by Les et al. (2010), Valen-Sendstad et al. (2011) and Arzania & Shaddenb (2012).

2   Computational methodology

The AAA geometry used in this study is generated from CT scans using the commercial medical imaging software Mimics. The geometry of the two patients, referred to as case 1 and case 2, is shown in figure 1. Case 1 has an AAA diameter approaching the size criterion of 5 cm and case 2 has a AAA diameter that has dilated to over 7 cm, well beyond the size threshold. For both cases, the aorta contorts as it leads into the AAA. To simplify the geometry, arteries that branch off of the aorta, such as the renal arteries, are excluded from the model and the upstream aorta is modeled as a constant diameter tube that transitions into the patient-specific aorta shape. The front and back sides of the AAA are referred to as anterior and posterior, respectively.

The period of a blood pulse is given by T and the phase position within the period is represented as $\phi(t) \in [0, T]$. The length scale is the upstream aorta radius R and velocity components are normalized by the time average of the bulk velocity $\overline{u}_b$, where an overbar indicates a flow quantity has been averaged over a blood pulse. The non-dimensional parameters that govern vascular flow are the bulk Reynolds number Re_b, Womersley number Wo and the max-to-mean flow rate ratio β defined as:

$$Re_b = 2\overline{u}_b R/\nu, \qquad (1)$$

$$Wo = R\sqrt{n/\nu}, \qquad (2)$$

$$\beta = u_{b,max}/\overline{u}_b. \qquad (3)$$

Here $\nu = \mu/\rho$ is the kinematic viscosity, with μ and ρ being the dynamic viscosity and density, respectively, $n = 2\pi/T$ is the frequency and the subscript max indicates the maximum value that occurs during a pulse. For this study, using flow conditions representative of the abdominal aorta, $Re_b = 390$, $Wo = 15.3$ and $\beta = 6.5$. Wo describes the phase-lag between the pressure gradient and the flow rate. In small arteries, where $Wo << 1$, the pressure gradient is aligned with the flow rate and it can be treated as quasi-steady. As Wo is increased, the flow rate begins to lag behind the pressure gradient and the velocity profile no longer matches Poiseuille flow. $Wo > 10$ is considered highly unsteady with inertia forces dominate over viscous forces (Ku 1997). The parameters used in this study are summarized in table 1.

An incompressible fluid with Newtonian properties is assumed. The governing equations for the conservation of mass and momentum, in a Cartesian coordinate system $\boldsymbol{x} = (x, y, z)$, are as follows:

Re_b	390	
Wo	15.3	
β	6.5	
ρ	1050	kg m^{-3}
μ	0.0035	kg m^{-1} s^{-1}
T	1	s
R	0.011	m
maximum flow rate	147.2	ml s^{-1}
mean flow rate	22.8	ml s^{-1}

Table 1: Summary of the parameters used in study.

$$\nabla \cdot \boldsymbol{u} = 0 \qquad (4)$$

$$\partial \boldsymbol{u}/\partial t + \boldsymbol{u} \cdot \nabla \boldsymbol{u} = -\nabla p + \nu \nabla^2 \boldsymbol{u} \qquad (5)$$

where the velocity field is given by $\boldsymbol{u} = (u, v, w)$, $p = P/\rho$, with P being the pressure.

The open source finite-volume code OpenFOAM-2.2.0 is used to directly solve the governing equations. To ensure the Courant-Friedrichs-Lewy (CFL) number < 1, the time step is fixed at $\Delta t = 0.5 \times 10^{-4}$ s during a pulse. The simulation is performed on 48 processors. The initial flow field is set to zero and statistics are collected after 10 pulses have been simulated to remove the effect of initial conditions. An unstructured grid composed of 3078214 and 4462192 tetrahedral and prism cells for case 1 and case 2, respectively, are generated using the commercial grid generation software Pointwise. The wall tangent and normal edge length of the first prism cell adjacent to the wall is given by $\Delta s_t = 0.005$ cm and $\Delta s_n = 0.075$ cm, respectively. Using the maximum WSS at the inlet boundary to scale the grid spacing in viscous units, $\Delta s_t^+ = 0.8$ and $\Delta s_n^+ = 11.6$. The superscript $^+$ denotes scaling with the viscous length ν/u_τ, where u_τ is the friction velocity. From the wall 14 prism cells are extruded at an expansion rate of 1.1. The tetrahedral cells that occupy the remaining of the domain have a viscous edge length of $\Delta s^+ = 11.6$.

Systole refers to when blood is ejected from the heart and diastole to when the heart muscle relaxes. The phase variation in the abdominal aortic flow rate used in this study is shown in figure 2 (a). The pulse profile originated from Les et. al. (2010) as discrete flow rate data and is expressed as a 12 term Fourier series. A fully developed unsteady velocity profile is calculated from the Fourier coefficients using procedures given in Womersley (1955), Hale et al. (1955), McDonald (1955) and Loudon and Tordesillas (1998). This profile is used as the inlet condition upstream in the aorta. Figure 2 (b) shows the phase variation in WSS at the inlet boundary. The highest WSS during the pulse is 2.8 N m^{-2} and occurs at $\phi/T = 0.17$. There is a phase-lag of $\phi/T = 0.02$ between the maximum WSS and maximum flow rate. As the flow
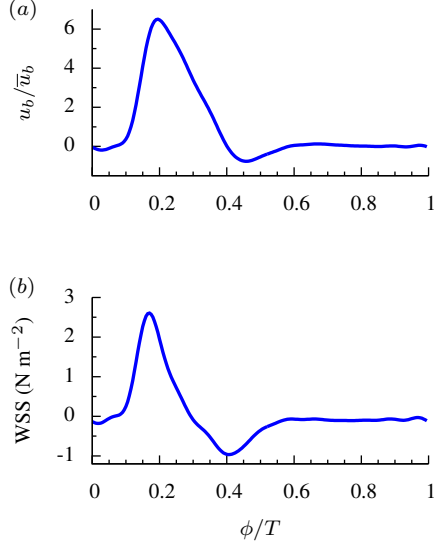
Figure 2: Phase variation at the inlet boundary in (a) $u_b/\overline{u}_b$ and (b) WSS.

decelerates during the later half of systole, the adverse pressure gradient causes the flow to separate at $\phi/T = 0.29$ resulting in negative WSS. The bulk flow does not decelerate to zero until $\phi/T = 0.40$ and reverses in direction during the start of diastole. The lowest WSS is -1.1 N m^2 and occurs at $\phi/T = 0.40$. During the later half of diastole, WSS and the bulk flow are effectively zero. Typically in arteries instantaneous WSS ranges from 1-7 N m^{-2} (Malek et al. 1999) and Dolan et al. (2012) classified high WSS as > 3 N m^{-2}. At the outlet boundaries, downstream in the iliac arteries, both inflow and outflow is allowed depending on the boundary flux. The arterial walls are assumed to be rigid with a no-slip condition.

Phase averaging procedure

Using the triple decomposition method introduced by Reynolds & Hussain (1970) a periodic flow quantity $f(\mathbf{x}, t)$ can be decomposed into

$$f(\boldsymbol{x}, t) = \overline{f}(\boldsymbol{x}) + \widetilde{f}(\boldsymbol{x}, \phi) + f'(\boldsymbol{x}, t), \qquad (6)$$

where $\overline{f}(\boldsymbol{x})$ is the time average, $\widetilde{f}(\boldsymbol{x}, \phi)$ is the periodic component and $f'(\boldsymbol{x}, t)$ is the turbulent component. Each blood pulse is segmented into $M = 25$ equidistant phase positions and at each phase $N = 50$ flow fields are collected. These values are limited by both computational and storage resources. The average of $f(\boldsymbol{x}, t)$ locked at a phase is calculated as

$$\left\langle f\left(\boldsymbol{x}, \phi\right) \right\rangle = \frac{1}{N} \sum_{i=0}^{N-1} f\left(\boldsymbol{x}, t + iT\right), \qquad (7)$$

with $\left\langle f\left(\boldsymbol{x}, \phi\right) \right\rangle$ being referred to as the phase average and is the sum of $\overline{f}(\boldsymbol{x})$ and $\widetilde{f}(\boldsymbol{x}, \phi)$. The instantaneous turbulent component can be calculated as
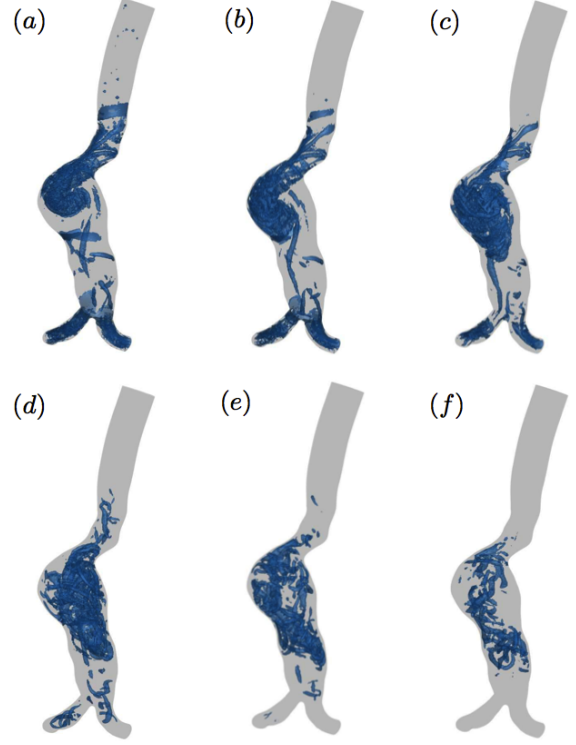

Figure 3: Case 1 isosurfaces of instantaneous coherent structures visualized by $-20\overline{u}_b^2/R^2$ using the λ_2 criterion: phase positions (a) $\phi/T = 0.28$, (b) $\phi/T = 0.32$, (c) $\phi/T = 0.40$, (d) $\phi/T = 0.56$, (e) $\phi/T = 0.72$ and (f) $\phi/T = 0.88$.

$$f'(\boldsymbol{x}, t) = f\left(\boldsymbol{x}, t\right) - \left\langle f\left(\boldsymbol{x}, \phi\right) \right\rangle \qquad (8)$$

and the time average of flow quantities is calculated as the summation of the phase-averaged quantities, where

$$\overline{f}(\boldsymbol{x}) = \frac{1}{M} \sum_{i=0}^{M-1} f(\boldsymbol{x}, \phi). \qquad (9)$$

3 Results

Figure 3 shows isosurfaces of instantaneous coherent structures for case 1 visualized by $-20\overline{u}_b^2/R^2$ using the λ_2 criterion of Jeong & Hussain (1995). Here λ_2 is the second largest eigenvalue of the the tensor $\mathbf{S}^2 + \mathbf{\Omega}^2$, where $\mathbf{S}$ and $\mathbf{\Omega}$ are the symmetric and antisymmetric components of the velocity gradient, respectively. During systole flow structures form at the AAA throat and by mid systole impinge against the arterial wall at the site of maximal aortic diameter. The structures spiral within the AAA, shearing against the arterial wall and breaking down into smaller turbulent structures. During diastole the bulk flow through the AAA is effectively zero but the turbulent structures continue to spiral making approximately 1.5 revolutions during a pulse. Since the diameter of the AAA is larger than the upstream aorta, the local Wo is higher,
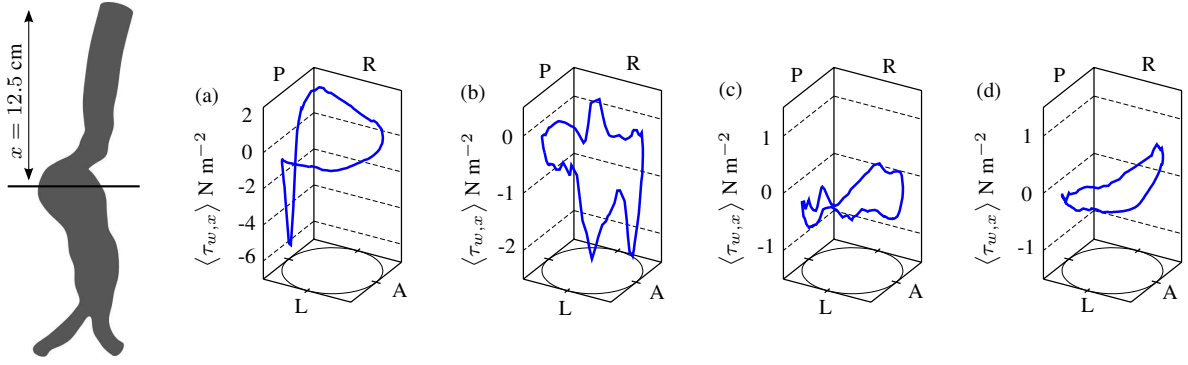
Figure 5: Case 1 $\langle \tau_{w,x} \rangle$ along the intersection of the arterial wall and a y-z plane at $x = 12.5$ cm: phase positions (a) $\phi/T = 0.24$, (b) $\phi/T = 0.4$, (c) $\phi/T = 0.56$ and (d) $\phi/T = 0.72$.
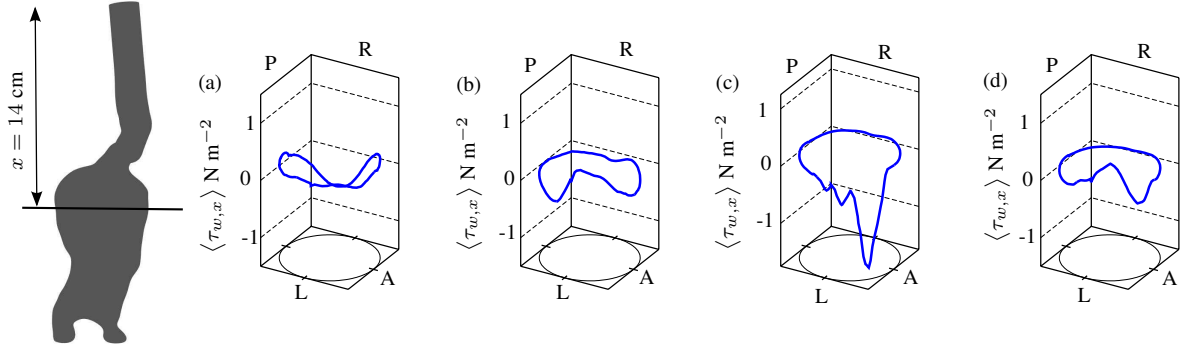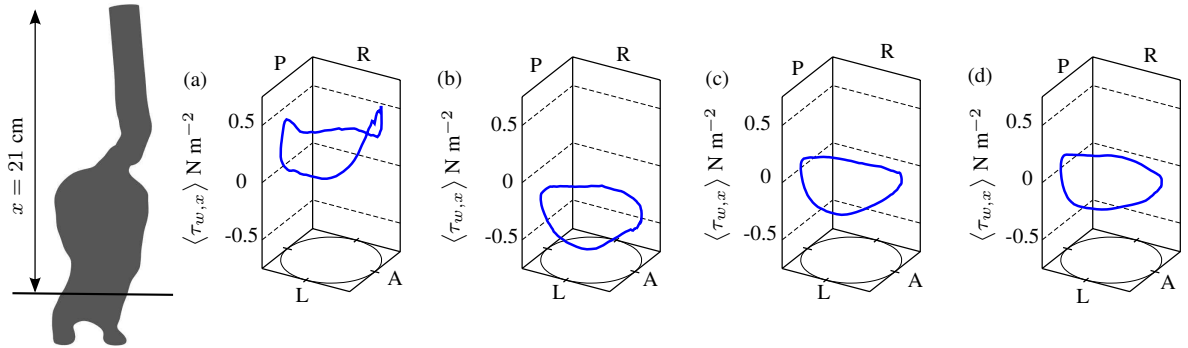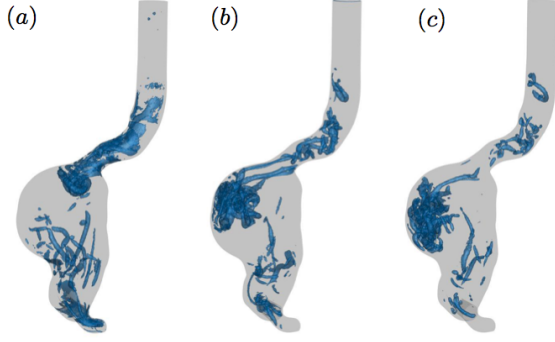

Figure 6: Case 2 $\langle \tau_{w,x} \rangle$ along the intersection of the arterial wall and a y-z plane at $x = 14$ cm: phase positions (a) $\phi/T = 0.24$, (b) $\phi/T = 0.4$, (c) $\phi/T = 0.56$ and (d) $\phi/T = 0.72$.

Figure 7: Case 2 $\langle \tau_{w,x} \rangle$ along the intersection of the arterial wall and a y-z plane at $x = 21$ cm: phase positions (a) $\phi/T = 0.24$, (b) $\phi/T = 0.4$, (c) $\phi/T = 0.56$ and (d) $\phi/T = 0.72$.

Figure 4: Case 2 isosurfaces of instantaneous coherent structures visualized by $-5\overline{u}_b^2/R^2$ using the λ_2 criterion: phase positions (a) $\phi/T = 0.32$, (b) $\phi/T = 0.60$ and (c) $\phi/T = 0.80$.
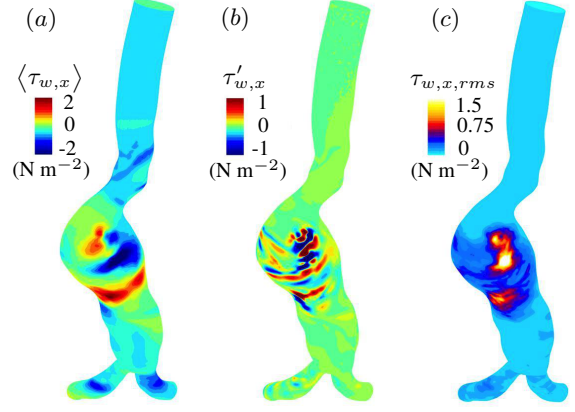

Figure 8: Case 1 surface contours of (a) $\langle \tau_{w,x} \rangle$, (b) $\tau'_{w,x}$ and (c) $\tau_{w,x,rms}$ at phase position $\phi/T = 0.4$.
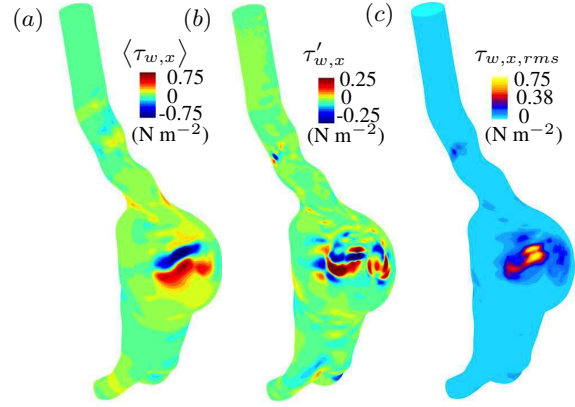

Figure 9: Case 2 surface contours of (a) $\langle \tau_{w,x} \rangle$, (b) $\tau'_{w,x}$ and (c) $\tau_{w,x,rms}$ at phase position $\phi/T = 0.56$.

increasing the prevalence of unsteady inertia forces in the AAA. At the start of diastole due to the reversal in bulk flow direction some of the coherent structures in the aorta are pulled upstream. By the end of diastole the turbulent structures are dissipating and the process begins again with the next pulse. Figure 4 shows isosurfaces of instantaneous coherent structures for case 2 visualized by $-5\overline{u}_b^2/R^2$ using the λ_2 criterion. Similar to case 1, flow structures form at the AAA throat but it is not until early diastole that the jet impinges against the arterial wall and breaks down into a turbulent flow. During diastole the turbulent structures continue to flow downstream, shearing along the anterior side of the AAA. Since the AAA is larger, relative to case 1, the structures are slower moving and it is not until systole of the next pulse that the structures are ejected from the AAA into the iliac arteries. Similar to case 1, the site of maximal aortic diameter is the location the structures impinge.

Figure 5 shows, for case 1, the phase-averaged x-component of the WSS, $\langle \tau_{w,x} \rangle$, along the intersection of the arterial wall and a y-z plane at $x = 12.5$ cm. The anterior, posterior, left and right sides are referred to as A, P, L and R, respectively. Phase averaging removes the instantaneous incoherent motion leaving the large-scale coherent structures. At $\phi/T = 0.24$ there is a sharp spike in $\langle \tau_{w,x} \rangle$ on the posterior side below the AAA throat. High $\langle \tau_{w,x} \rangle$ only occurs briefly at this location and by $\phi/T = 0.4$ the flow structures have spiraled to the anterior side and $\langle \tau_{w,x} \rangle$ has decreased in magnitude. For the remainder of the pulse $\langle \tau_{w,x} \rangle$ is relatively low along the slice and fluctuates between positive and negative values. Figure 6 shows for case 2 $\langle \tau_{w,x} \rangle$ along the intersection of the arterial wall and a y-z plane at $x = 14$ cm. A sharp spike in $\langle \tau_{w,x} \rangle$ is shown to occur on the left anterior side at $\phi/T = 0.56$. Figure 7 shows for case 2 $\langle \tau_{w,x} \rangle$ along the intersection of the arterial wall and a y-z plane at $x = 21$ cm. This slice is located slightly above the iliac arteries and here $\langle \tau_{w,x} \rangle$ is relatively uniform along the arterial wall. This indictates that the large-scale

structures that form at the AAA's throat do not interact with this downstream location. Along the slice $\langle \tau_{w,x} \rangle$ changes from positive, negative or $\approx$ zero with the expected WSS value from figure 2 (b).

Surface contours of WSS are shown for case 1 at $\phi/T = 0.4$ and case 2 at $\phi/T = 0.56$ in figure 8 and 9, respectively. It can be seen in figure 8 (a) and figure 9 (a) large structures of positive and negative $\langle \tau_{w,x} \rangle$ shear across the AAA with the magnitude of $\langle \tau_{w,x} \rangle$ being higher for case 1. Figure 8 (b) and figure 9 (b) show the instantaneous incoherent WSS x-component $\tau'_{w,x}$. For both cases fluctuations in $\tau'_{w,x}$ are localized to the proximity of the large structures and follows the structures movement as they shear across the AAA. Figure 8 (c) and figure 9 (c) show the phase-averaged quantity $\tau_{w,x,rms}$, where the subscript rms indicates the operation $\langle \sqrt{f'f'} \rangle$. For case 1, $\tau_{w,x,rms}$ occupies a larger surface area of the AAA and is at a higher intensity, relative to case 2.

The phase-averaged turbulent kinetic energy is defined as $\langle \text{TKE} \rangle = 1/2 \langle \boldsymbol{u'} \cdot \boldsymbol{u'} \rangle$. Figure 10 shows for case 1 $\langle \text{TKE} \rangle / \overline{u}_b^2$ on a x-z plane at $y = 5.3$ cm. High TKE is not present in the AAA until late systole and it
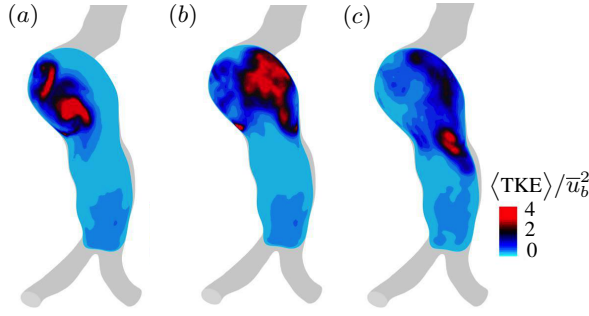
Figure 10: Case 1 contours of $\langle \text{TKE} \rangle / \overline{u}_b^2$ on a x-z plane at $y = 5.3$ cm: phase positions (a) $\phi/T = 0.36$, (b) $\phi/T = 0.44$ and (c) $\phi/T = 0.52$.
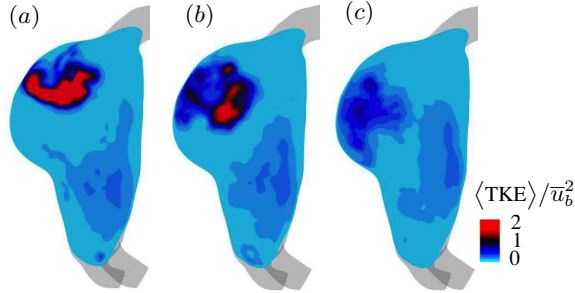

Figure 11: Case 2 contours of $\langle \text{TKE} \rangle / \overline{u}_b^2$ on a x-y plane at $x = 1.6$ cm: phase positions (a) $\phi/T = 0.48$, (b) $\phi/T = 0.60$ and (c) $\phi/T = 0.80$.

Figure 12: Case 1 temporal variation in $u/\overline{u}_b$ at probe locations (a) $\mathcal{P}1$ and (b) $\mathcal{P}2$ during the last three simulated pulses.

Figure 13: Case 2 temporal variation in $u/\overline{u}_b$ at probe locations (a) $\mathcal{P}3$ and (b) $\mathcal{P}4$ during the last three simulated pulses.

spirals within the AAA following the path of the flow structures. During diastole $\langle \text{TKE} \rangle / \overline{u}_b^2$ dissipates in intensity. Figure 11 shows for case 2 $\langle \text{TKE} \rangle / \overline{u}_b^2$ on a x-y plane at $x = 1.6$ cm. High TKE is not present in the AAA until early diastole and similar to case 1 the TKE follows the path of the flow structures and dissipates during late diastole. Case 2 has a zone of $\langle \text{TKE} \rangle / \overline{u}_b^2$ on its posterior side that persists at a low intensity throughout diastole. For both cases there is a phase-lag between the highest flow rate and the formation of TKE, but this phase-lag is more profound for case 2.

The turbulent component in the flow is further investigated by viewing the velocity signal at discrete locations in the AAA. For case 1 $\mathcal{P}1 = (12, 4, 2)$cm and $\mathcal{P}2 = (12, 5, 2)$cm are probes located within the AAA's bulge. Figure 12 shows the temporal variation in $u/\overline{u}_b$ at these probe locations during the last three simulated pulses. At both probe locations, there is a distinct coherent component to the velocity signal that repeats every period and an incoherent or turbulent component. The turbulent component at $\mathcal{P}2$ qualitatively appears to be at a higher intensity, relative to $\mathcal{P}1$. Figure 13 shows for case 2 $u/\overline{u}_b$ at $\mathcal{P}3 = (15, 8, 2)$cm and $\mathcal{P}4 = (18, 5, 2)$cm during the last three simulated pulses. $\mathcal{P}3$ is located on the anterior side in the path of the flow structures and $\mathcal{P}4$ is located on the posterior
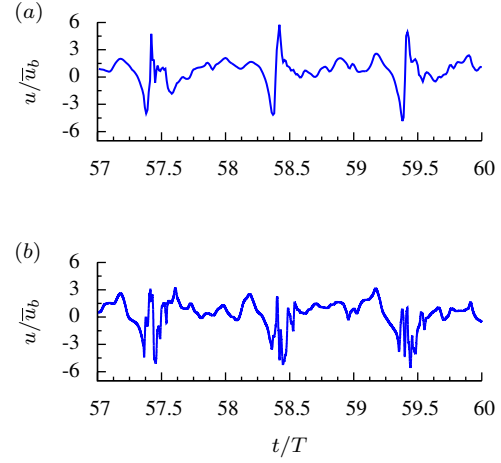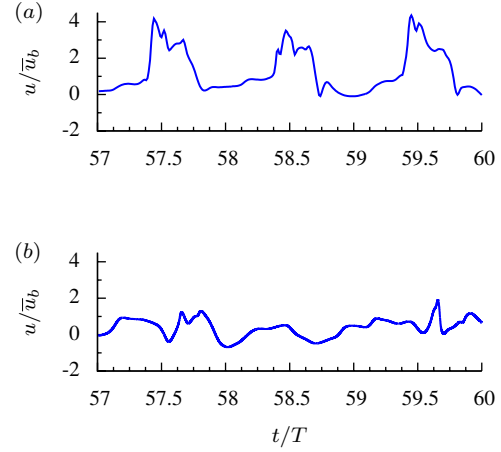
side. It can be seen qualitatively at $\mathcal{P}3$ the turbulent component is at a lower intensity and frequency, relative to the case 1 probes. At $\mathcal{P}4$ there is no distinct coherent motion to the velocity signal and qualitatively it appears to be dominated by low-frequency turbulent fluctuations. In figure 14 for case 2 at $\mathcal{P}3$ the velocity is decomposed into its instantaneous turbulent component $u'/\overline{u}_b$ and plotted over the last 10 simulated pulses. By viewing $u'/\overline{u}_b$ it can not be determined where in the period of the pulse the highest turbulent intensity would occur. In figure 15 phase averaging has been applied to the instantaneous turbulent component and $\langle \text{TKE} \rangle / \overline{u}_b^2$ has been calculated at $\mathcal{P}3$. It can be seen that the highest $\langle \text{TKE} \rangle / \overline{u}_b^2$ does not occur until late diastole and is $\approx$ zero during systole.

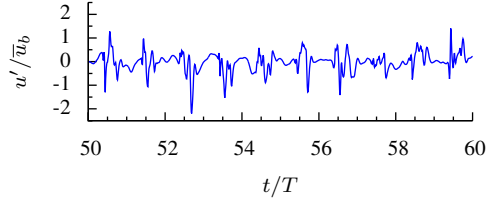The time-averaged streamlines are shown for case 1 in figure 16 (a) and case 2 in figure 16 (b). Time

Figure 14: Case 2 temporal variation in $u'/\overline{u}_b$ at probe location $\mathcal{P}3$ during the last 10 simulated pulses.
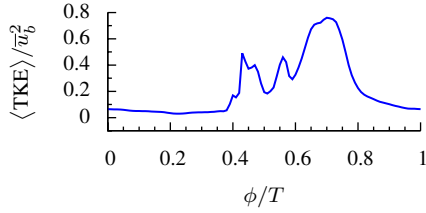

Figure 15: Case 2 phase variation in $\langle \text{TKE} \rangle/\overline{u}_b^2$ at probe location $\mathcal{P}3$.

averaging removes the time-dependent flow structures and gives an overall description of the flow field and the hemodynamic forces acting on the arterial wall. For case 1 the time-averaged flow field consists of a jet that impinges against the arterial wall and spirals down the length of the AAA. There is no zone of separated recirculating flow for case 1. The time-averaged streamlines for case 2 show that the flow also impinges against the arterial wall, however instead of spiraling like case 1, the blood flows downstream on the anterior side and a large zone of recirculating blood forms on the posterior side. For both cases the AAA bulges at the location the time-averaged streamlines impinge.

The time-averaged TKE is shown for case 1 on a x-z plane at y = 5.3 cm in figure 15 (a) and case 2 on a x-y plane at x = 1.6 cm in figure 15 (b). It can
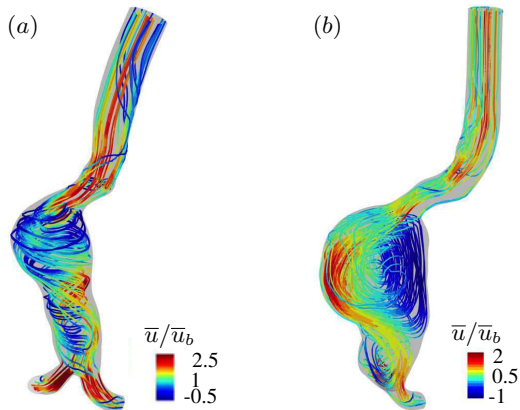

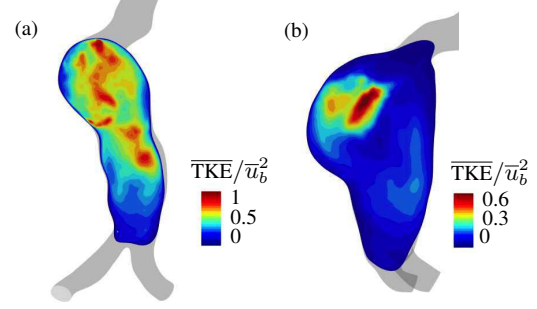Figure 16: Time-averaged streamlines for (a) case 1 and (b) case 2.

Figure 17: Contours of $\overline{\text{TKE}}/\overline{u}_b^2$ for (a) case 1 on a x-z plane at $y/R = 4.8$ and (b) case 2 on a x-y plane at $x/R = 1.4$.

be seen that for case 1, high $\overline{\text{TKE}}/\overline{u}_b^2$ occupies a majority of the AAA's volume and the highest $\overline{\text{TKE}}/\overline{u}_b^2$ occurs along the centre axis of the AAA. For case 2 a zone of high $\overline{\text{TKE}}/\overline{u}_b^2$ occurs on the anterior side in the AAA's bulge and occupies a relatively small amount of the total AAA volume. A smaller zone of lower intensity $\overline{\text{TKE}}/\overline{u}_b^2$ occurs on the posterior side. Overall $\overline{\text{TKE}}/\overline{u}_b^2$ for case 1 it is significantly higher and occupies at larger amount of the total AAA volume, relative to case 2.

4   Conclusions

Direct numerical simulation has been performed on two patient-specific AAA. The hemodynamics vary considerably between the cases and the flow is found to be comprised of complex periodic and turbulent structures. To analyze the phase-variation during a pulse the velocity was decomposed into it's instantaneous turbulent and phase-averaged component. For both cases the blood flow transitions from laminar-to-turbulent and back to laminar during a pulse. There is considerable phase-lag between the maximum flow rate and the formation of turbulent flow structures in the AAA. During systole, for both cases, a jet forms at the AAA's throat and impinges against the arterial wall with the AAA appearing to bulge at the impingement location. During diastole, when the bulk flow through the AAA is $\approx$ zero, the velocity in the AAA is not zero and the flow structures continue to shear across the arterial wall. High WSS and TKE occurs in the proximity of the flow structures. The following differences exist between the two cases:

- For case 1 the flow transitions-to-turbulence during late systole and for case 2 during early diastole. For both cases the turbulence has mostly dissipated by early systole of the next pulse.

- Overall the flow velocity is higher in case 1's AAA. This results in faster moving flow structures, higher WSS and TKE. High TKE occupies a larger amount of the AAA volume for case 1.

- For case 1 the blood flow spirals within the AAA and for the time-averaged flow there is no zone of separated recirculating blood. For case 2 the blood flows downstream on the anterior side and a large zone of recirculating blood forms on the posterior side.

Within the scope of the two AAA studied here the moderately sized AAA has higher turbulence and WSS. However the larger-sized AAA has a large recirculation zone which is not present in the moderately-sized AAA. Physiologically both high turbulence and a large recirculation zone could damage the arterial wall.

Acknowledgments

References

Arzani, A., Shadden, S.C. (2012), Characterization of the transport topology in patient-specific abdominal aortic aneurysm models, *Phys. Fluids*, Vol. 24, pp. 1-16.

Dolan, J.M., Kolega, J., Meng, H. (2012), High wall shear stress and spatial gradients in vascular pathology: A review, *Ann. Biomed. Eng.*, Vol. 41, pp. 1411-1427.

Hale, J.F., McDonald, D.A., Wormersley, J.R. (1955), Velocity profiles of oscillating arterial flow, with some calculations of viscous drag and the Reynolds number, *J. Physiol.*, Vol. 128, pp. 629-640.

Hussain, A.K.M.F., Reynolds, W.C. (1970), The mechanics of an organized wave in turbulent shear flow, *J. Fluid Mech.*, Vol. 41, pp. 241-258.

Jeong, J., Hussain, F. (1995), On the identification of a vortex, *J. Fluid Mech.*, Vol. 285, pp. 69-94.

Ku, D.N. (1997), Blood flow in arteries, *Annu. Rev. Fluid Mech.*, Vol. 29, pp. 399-434.

Lasheras, J.C. (2010), Haemodynamic stresses and the onset and progression of vascular diseases, *J. Fluid Mech.*, Vol. 664, pp. 1-4.

Les, A.S., Shadden, S.C., Figueroa, C.A., Park, J.M., Tedesco, M.M., Herfkens, R.J., Dalman, R.L., Taylor, C.A. (2010), Quantification of hemodynamics in abdominal aortic aneurysms during rest and exercise using magnetic resonance imaging and computational fluid dynamics, *Ann. Biomed. Eng.*, Vol. 38, pp. 12881313.

Les, A.S., Yeung, J.J., Schultz, G.M., Herfkens, R.J., Dalman, R.L., Taylor, C.A. (2010), Supraceliac and infrarenal aortic flow in patients with abdominal aortic aneurysms: mean flows, waveforms, and allometric scaling relationships, *Card. Eng. Tech.*, Vol. 1, pp. 39-51.

Loudon, C., Tordesillas, A., (1998), The use of the dimensionless womersley number to characterize the unsteady nature of internal flow, *J. theor. Biol.*, Vol. 191, pp. 63-78.

McDonald, D.A., (1955), The relation of pulsatile pressure to flow in arteries, *J. Physiol.*, Vol. 127, pp. 533-552.

Stamatopoulos, C., Mathioulakis, D.S., Papaharilaou, Y., Katsamouris, A. (2010), Experimental unsteady flow study in a patient-specific abdominal aortic aneurysm model, *Exp. Fluids*, Vol. 50, pp. 1695-1709.

Tarbell, J.M., Shi, Z., Dunn, J., Jo, H., (2014), Fluid mechanics, arterial disease, and gene expression, *Annu. Rev. Fluid Mech.*, Vol. 46, pp. 591-614.

Valen-Sendstad, K., Mardal, K., Mortensen, M., Reif, B.A.P., Langtangen, H.P., (2011), Direct numerical simulation of transitional flow in a patient-specific intracranial aneurysm *J. Biomech.*, Vol. 44, pp. 2826-2832.

Wormersley, J.R. (1955), Method for the calculation of velocity, rate of flow and viscous drag in arteries when the pressure gradient is known, *J. Physiol.*, Vol. 127, pp. 553-563.